PHYSICAL REVIEW C VOLUME 55, NUMBER 5 MAY 1997

Pion shadowing as a tool to study the topology of heavy-ion collisions at intermediate energies

A. Badalà,[1] R. Barbera,[1,2] A. Palmeri,[1] G. S. Pappalardo,[1] F. Riggi,[1,2] A. C. Russo,[1] G. Russo,[2,3] and R. Turrisi[1,2]

[1]*Istituto Nazionale di Fisica Nucleare, Sez. di Catania Corso Italia, 57-I 95129 Catania, Italy*
[2]*Dipartimento di Fisica dell'Università di Catania Corso Italia, 57-I 95129 Catania, Italy*
[3]*Istituto Nazionale di Fisica Nucleare, Laboratorio Nazionale del Sud Via Santa Sofia, 44-I 95123 Catania, Italy*

(Received 15 January 1996; revised manuscript received 26 November 1996)

The pion reabsorption effect has been exploited, through a new analysis technique, to study the topological distribution of nuclear matter in the course of a heavy-ion collision at intermediate energies. The azimuthal angular distribution of pions with respect to the reaction plane and the angular correlations between pions and projectilelike fragments have been investigated. Quantitative estimations of the pion production time scale and of the impact parameter range involved are provided. The experimental results are successfully compared with the predictions of a microscopic theoretical model based on the solution of the Boltzmann-Nordheim-Vlasov transport equation. [S0556-2813(97)00504-9]

PACS number(s): 25.70.−z, 21.65.+f, 24.10.Nz

I. INTRODUCTION

The study of heavy-ion collisions at intermediate bombarding energies represents a unique tool to investigate the complex interplay between the attractive action of the nuclear mean field and the repulsive one due to nucleon-nucleon collisions. One of the most interesting challenges to this kind of physics is the determination, as a function of time, of the spatial distribution of the nuclear matter present all around the reaction site. The knowledge, as the reaction proceeds, of where the matter is and how excited it is, is in fact of extreme importance in the understanding of the final distributions of the physical observables.

In the analysis presented in this paper we tried to pursue this aim, taking advantage of the fact that π mesons, which are created in the early stages of a heavy-ion collision at intermediate energies [1,2], are strongly interacting with the surrounding nuclear matter. They can be rescattered and/or reabsorbed with probabilities which are functions of their kinetic energy and of the size and excitation energy of the systems which they interact with [3–7]. The existence of this final state interaction, which has been so far claimed as one of the most important drawbacks in using pions as probes of the collision dynamics, has been here exploited, through new techniques, as an advantage to study the topological distribution of nuclear matter in the course of a heavy-ion collision at intermediate energies.

The next section is devoted to a description of the experimental setup, while Sec. III contains a review of the results concerning the azimuthal angular distribution of pions with respect to the reaction plane and the angular correlations between pions and projectilelike fragments. In Sec. IV the predictions of a microscopic theoretical model are compared with the data. A summary and conclusions are given in Sec. V.

II. EXPERIMENTAL SETUP

A view of a section of the used experimental setup with a plane containing the beam axis is shown in Fig. 1. It basically consists of the MEDEA multidetector [8] coupled with a two-ring hodoscope of 16 plastic scintillators which was added to cover the very forward angular range with respect to the beam direction.

The experiment has been performed at the GANIL facility using an ^{36}Ar beam at 95 MeV/nucleon impinging on ^{27}Al and ^{112}Sn targets whose thicknesses were 1.6 mg/cm^2 and 0.8 mg/cm^2, respectively.

A. MEDEA multidetector

In the experiment discussed in this article the MEDEA multidetector was made up of a ball of 144 BaF$_2$ scintillators (22 cm inner radius and 42 cm outer radius), arranged in six rings and covering the whole azimuthal dynamics between $\theta = 42°$ and $\theta = 138°$, and of a wall of 120 *phoswich* detectors (2 mm+30 cm total thickness), arranged in five rings and covering the whole azimuthal dynamics between $\theta = 10°$ and $\theta = 30°$.

1. Phoswich wall

In the forward-angle phoswhich detectors particle identification has been carried out by means of the usual shape analysis of the analog signal [8]. Two gates, the first one of about 20 ns (called *fast*) and the second one of about 1 μs

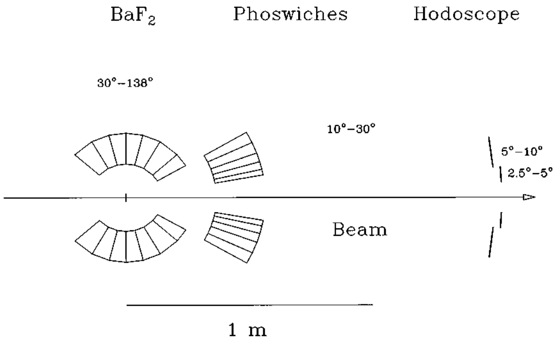

FIG. 1. A view of a section of the experimental setup with a plane containing the beam axis.

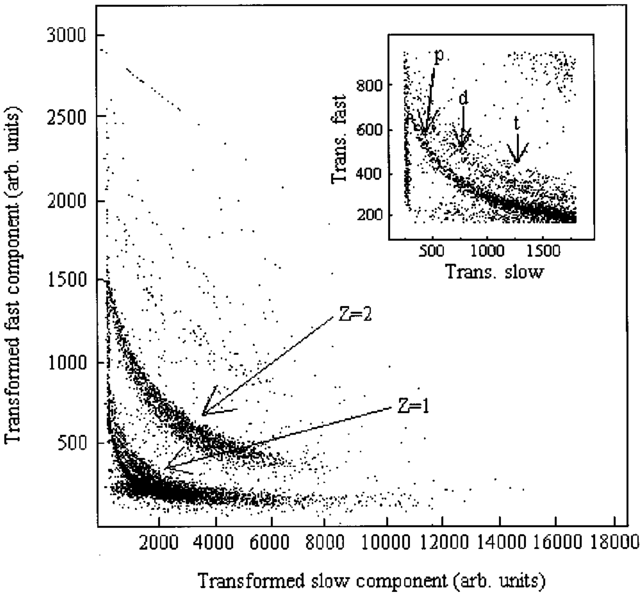

FIG. 2. *Fast-slow* scatter plot relative to a detector of the phoswich wall. The word ''transformed'' means that both *fast* and *slow* components have been suitably linearly rescaled to make the plot orthonormal.

(called *slow*), have been used to integrate the ionization charge produced inside the detector by the hitting particles. As an example, Fig. 2 shows the *fast-slow* scatter plot relative to a module of the detector. Charge states from $Z=1$ up to $Z=4$ are clearly visible and easily separable. In the small inset, relative to a zoomed portion of the lower left corner of the whole figure, $Z=1$ isotopes are also distinguishable.

Energy calibration has been achieved, for low-energy particles ($v<6$–7 cm/ns, depending on the particle), starting from time-of-flight measurements and, for high-energy particles, using momentum-tagged secondary beams of charged particles (the so-called $B\rho$ technique in use at the GANIL facility where the experiment was performed). At low particle energies, energy resolution is mostly due to the time resolution of the beam pulse which was about 800 ps full width at half maximum (FWHM), while at high particle energies the error in the energy assignment is due to the error inherent in the applied method. Typical values of (10–15)% in the low-energy range and (2–4)% in the high-energy one have been determined, as a function of the charge of the particle. The ''punch-in'' energy threshold, due to the finite thickness of the thinnest element of the phoswhich, is about 15 MeV for protons, 60 MeV for $Z=2$ particles, and so on for heavier fragments.

For hydrogen isotopes, which are directly identified in Fig. 2, the mass assignment posed, of course, no problem. For heavier fragments, the mass of the most abundant isotope has been (as usual) assigned to a given charge. The few $Z>4$ particles have been assumed to have $Z=5$ and a mass equal to 10 mass units.

2. *BaF$_2$ ball*

In the ball of barium fluoride detectors particle identification has been accomplished coupling the *fast-slow* technique (whose application is made possible here by the existence of two well-separated decay times of the BaF$_2$ crystal) with the time-of-flight information. Two differently attenuated *slow* signals (*slow1* and *slow2*), belonging to two contiguous regions of the whole energy dynamics, have been separately digitized [8]. Typical *fast-slow* and *time-total* (*total* = *slow1* + K × *slow2*) scatter plots relative to an element of the detector are shown in Fig. 3 and Fig. 4, respectively. Photons, which stay above the line drawn in Fig. 3 and below that one drawn in Fig. 4, appear very well separated from neutrons and charged particles (the photon peak in the time-

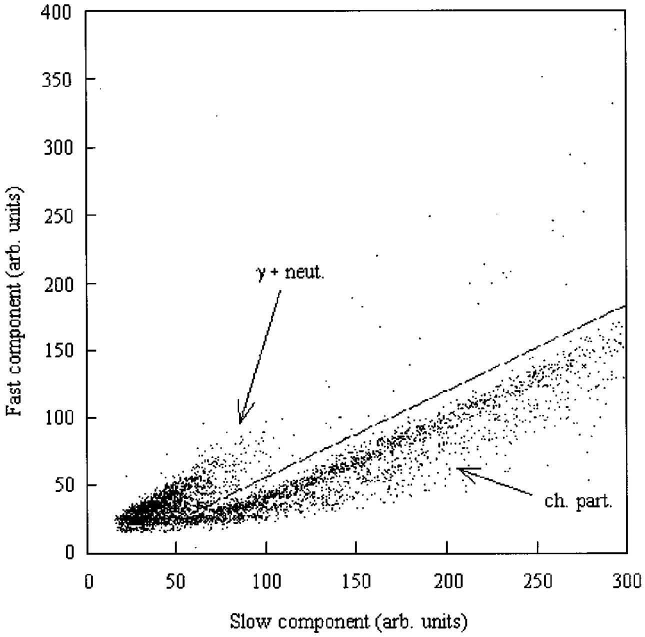

FIG. 3. *Fast-slow* scatter plot relative to a detector of the BaF$_2$ ball.

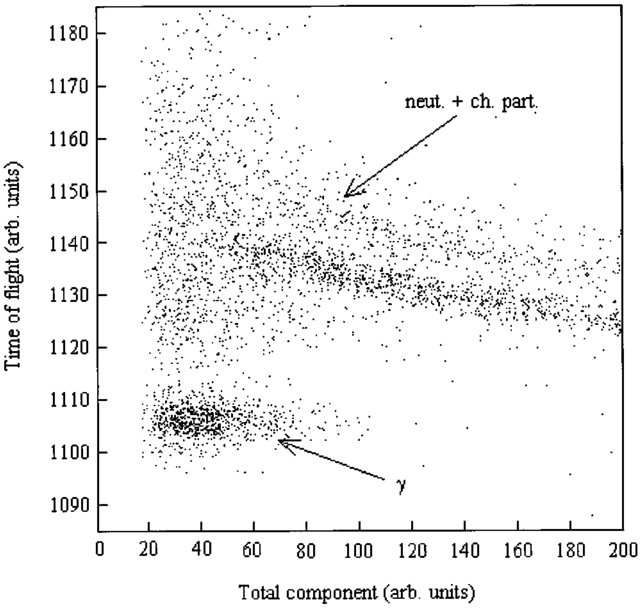

FIG. 4. *Time-total* scatter plot relative to a detector of the BaF$_2$ ball.

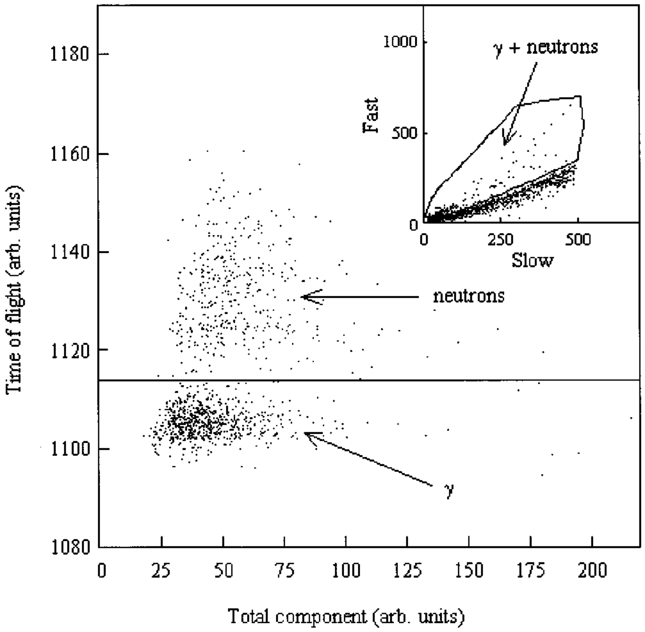

FIG. 5. *Time-total* scatter plot relative to a detector of the BaF_2 ball. Only those events having *fast-slow* coordinates falling inside the contour drawn in the inset of the figure have been plotted.

of-flight spectrum has a total width of about 2 ns). Hydrogen isotopes are clearly visible and fragments with charge $Z=2$ have been correctly identified and separated. For the BaF_2 ball we adopted the same charge-to-mass correspondence as for the phoswhich wall and we have assigned $Z=3$ and a mass equal to 7 mass units to the small amount of unidentified $Z>2$ fragments. Neutron/photon separation is also shown in Fig. 5 where the *time-total* scatter plot is reported for those events having *fast-slow* coordinates falling inside the contour drawn in the inset of the figure.

Charged particles have been calibrated in energy using the same $B\rho$ technique cited before. The calibration for low-energy particles ($E<25$ MeV) has been slightly scaled in accordance with Ref. [9] in order to take into account quenching effects. The low-energy cutoff in the case of the ball counters is about 10 MeV for protons and about 25 MeV for $Z=2$ fragments which represent together almost all particles detected in the ball. The problem of energy resolution in the the BaF_2 ball of MEDEA has been deeply analyzed [10]. Realistic values of (2–4)% have been found in the experiment discussed in the present article which are in agreement with those reported in Ref. [10].

The γ rays are detected in the BaF_2 ball of MEDEA simply by means of the calorimetric collection of the electromagnetic showers they induce into the detector material. The determination of the energy and angles of the detected photons is carried out using the following procedure. All modules having a value of the deposited energy different from zero are scanned in order to find the ''most-touched'' detector (i.e., with the highest value of the deposited energy). Let us call it $(i_{\max},j_{\max})$, where the index i ($i=1,2,\ldots,24$) is an order parameter running over the elements of one ring and the index j ($j=1,2,\ldots,6$) is an order parameter running over the useful rings of the ball. When this detector is found the analysis code looks at all detectors, verifying the relation $(i_{\max}-i)^2+(j_{\max}-j)^2\leq 2$ in order to determine whether or not the electromagnetic shower spreads out in these neighboring modules. If none with a deposited energy greater than its threshold is found, the photon energy is fixed equal to the deposited energy in the central detector and the polar and azimuthal detection angles are uniformly randomized within that detector. Otherwise, as is mostly the case, the energy of the photon-induced shower is obtained by summing over all elements of the cluster and the photon detection angles are evaluated as the averages of the corresponding (randomized) angles of the single detectors of the cluster, weighted over the deposited energy in each cluster element. When the energy and the detection angles of the first shower are determined and the shower multiplicity is greater than 1, the first ''most-touched'' detector and the involved neighboring modules are excluded from the loop and the program starts again to find a new ''most-touched'' detector. As has been shown in Refs. [8,11], this kind of procedure minimizes the sideward leakages of the shower (the full side dimension of each detection module is nearly twice the Molière radius of barium fluoride), ensuring a good estimate of the detector response to photons. In order to considerably reduce the background due to neutrons, the condition that the energy deposited in the central detector only must be larger than 20 MeV is also applied to the data.

The energy calibration for photons has been carried out using both a 6.13-MeV γ-ray PuC source and the value of the energy deposited by cosmic rays entering the detectors along their longest side (the energy loss of those minimum ionizing particles is about 6.7 MeV/cm for the BaF_2). The energy dynamics in which photons have been detected and identified spans from about 20 MeV to 230–250 MeV. The response function of the ball counters of MEDEA to energy-tagged photons has been experimentally determined [12] and successfully compared with Monte Carlo simulations [11,12].

Neutral pions have been detected in the whole solid angle and in the kinetic energy range between 0 and about 120 MeV through the simultaneous detection of the couples of photons coming from their main decay mode [$\pi^0\rightarrow 2\gamma$, branching ratio (BR)=98.8%]. These photons are separated from other pairs by imposing severe conditions on the experimental distributions of the relative angle θ_{12} and invariant mass m_{inv} as functions of the total energy E_1+E_2 of the two detected photons which are reported, for the ^{27}Al target, in the upper panel and in the lower panel of Fig. 6, respectively. The cuts drawn in both panels of Fig. 6 select those photons coming from π^0 decay and derive from the results of full GEANT3 [13] simulations performed to determine the detector efficiency $\epsilon(E_\pi,\theta_\pi)$ as a function of the pion kinetic energy and detection angle [11] (see Fig. 7). It is worth stressing here that all π-event distributions reported in this paper have been corrected for pion efficiency and the errors have been propagated accordingly. From a technical point of view this means that to plot all distributions reported in Figs. 10–12, 14–18, and 20–23 each event has not been included with a weight equal to 1 but equal to $1/\epsilon(E_\pi,\theta_\pi)$. The capability of the MEDEA multidetector as a photon and neutral pion spectrometer has been both extensively simulated [11,12,14–16] and experimentally verified [7,8,14–17]. The reader is then referred to those papers for more details.

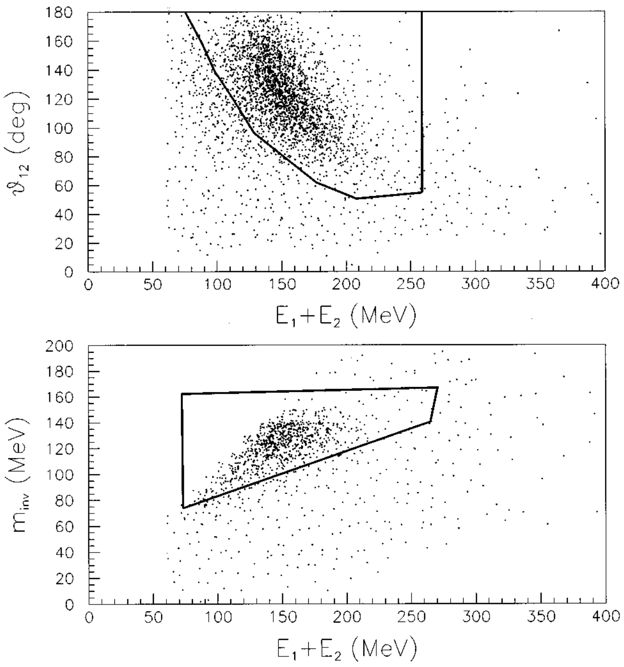

FIG. 6. Relative angle (upper panel) and invariant mass (lower panel) versus total energy distributions of the pairs of photons detected in the reaction ^{36}Ar+^{27}Al at 95 MeV/nucleon. In both plots, the contours defined by full GEANT simulations (see text) select those pairs of photons coming from π^0 decay.

Only as an example, which also gives an independent check of the energy calibration, Fig. 8 shows the comparison between the experimental invariant-mass distribution and that obtained by the simulation. The FWHM of the distribution is about 18% of the neutral pion rest mass ($m_{\pi^0}=135$ MeV).

B. Hodoscope

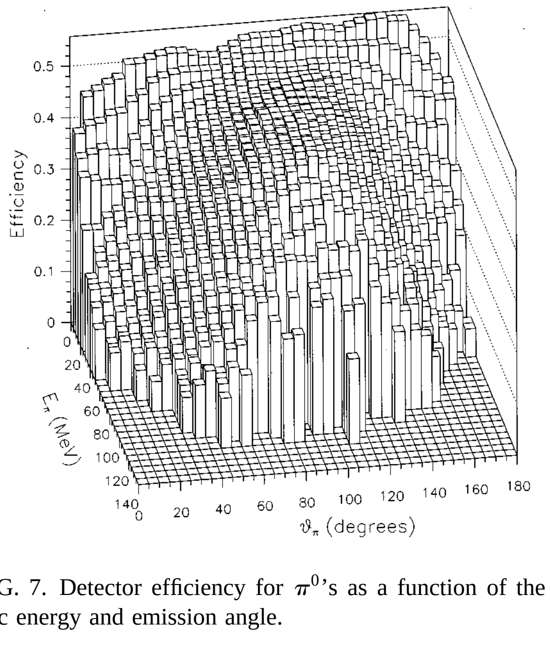

FIG. 7. Detector efficiency for π^0's as a function of the pion kinetic energy and emission angle.

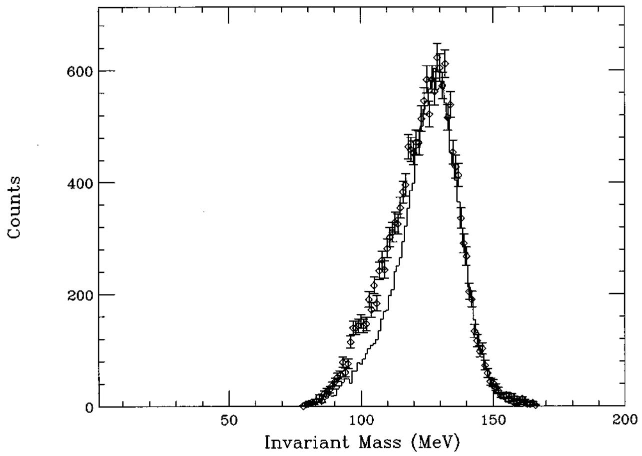

FIG. 8. Two-photon invariant-mass distribution relative to the system ^{36}Ar+^{27}Al. The histogram is the result of full GEANT simulations.

The forward hodoscope consisted of 16 2-mm-thick plastic scintillators arranged in two rings placed around the beam axis and divided into eight sectors each. The distance from the target was 150 cm so that the first ring covered the polar angles between $\theta=2.5°$ and $\theta=5°$ and the second one those between $\theta=5°$ and $\theta=10°$.

Charged particles were detected and identified by measuring both the energy loss and the time of flight. Figure 9 shows the scatter plot of the energy loss as a function of the time of flight for an element of the hodoscope. Fragments with charges between $Z=1$ and $Z=8$ are directly visible. Heavier fragments with $9\leqslant Z\leqslant 20$ have been tagged using a rough energy-loss calibration. The upper limit of $Z=20$, two units larger than the projectile charge, has been fixed in agreement with the existing systematics of experiments where the mass of the fragments has been directly measured. The charge uncertainty Σ using this procedure can be esti-

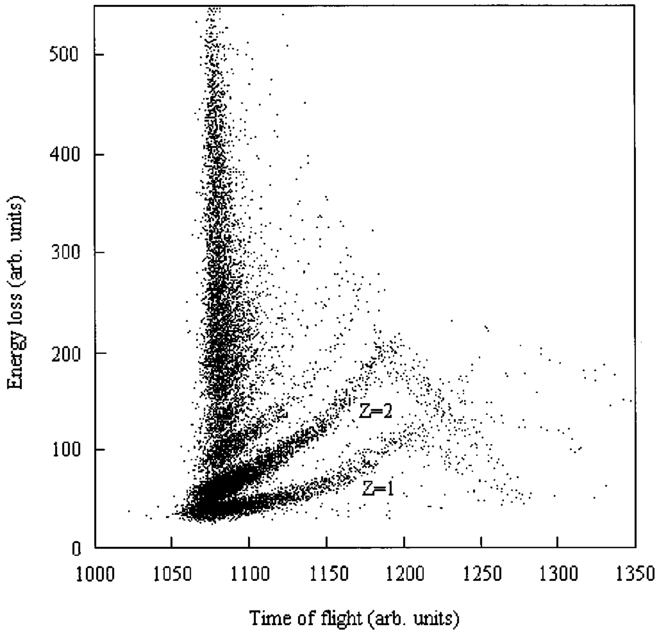

FIG. 9. Scatter plot of the time of flight vs energy loss for a detector of the hodoscope.

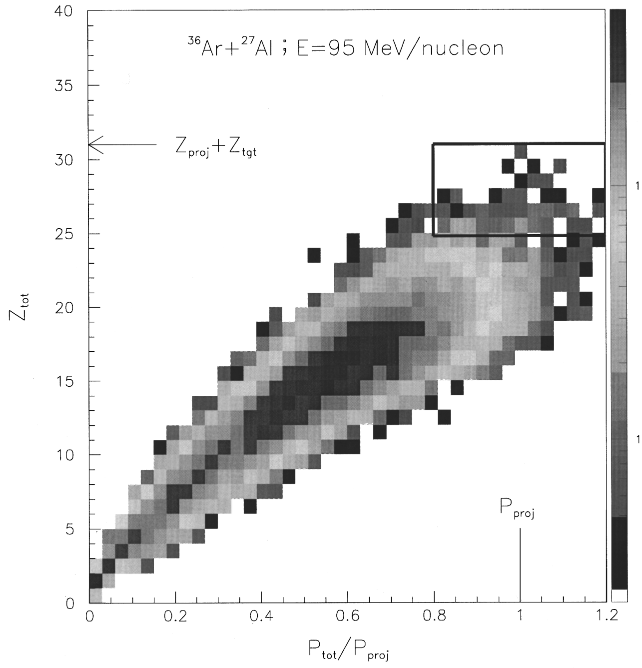

FIG. 10. Event distribution as function of the total detected charge and linear momentum (normalized to the projectile one). Data are relative to the ^{27}Al target.

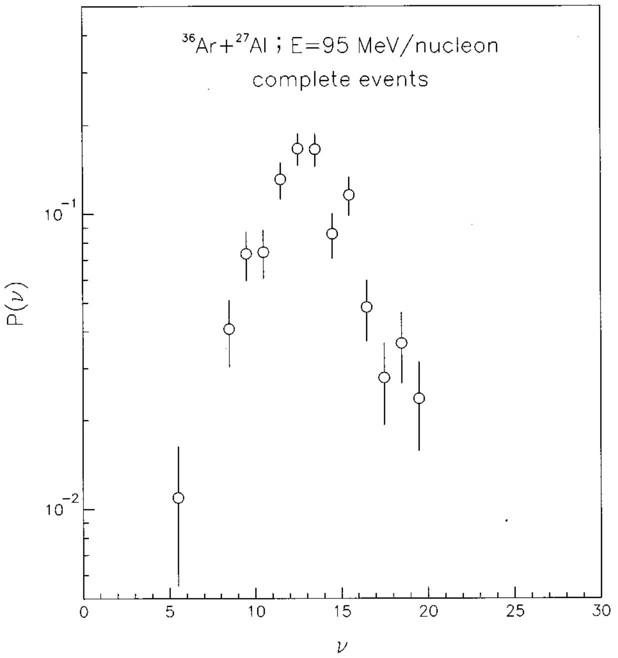

FIG. 12. Charged particle multiplicity distribution for *complete* events.

mated to be equal to two charge units. Also in this case the mass of the most abundant isotope has been assigned to a given charge.

The energies of the particles have been determined starting from their velocities and an absolute calibration has been obtained using the known time-of-flight values of the ‘‘punch-in’’ $Z=1$ and $Z=2$ fragments. The energy resolution, essentially due to the width of the rf signal, takes values between 10% and 20% going from the highest to the lowest energies.

C. Trigger

In the present paper only those events where a pion or a high-energy photon ($E_\gamma>30$ MeV) are detected in coincidence with at least one charged particle have been kept for further analysis. This latter condition has been imposed to eliminate the background induced by the cosmic radiation as it has been discussed in greater detail in Ref. [15].

III. RESULTS

A. Pion angular distribution with respect to the reaction plane

In recent years at least three different methods have been established to determine the reaction plane in a heavy-ion collision: the sphericity tensor method [18], the transverse momentum analysis [19], and the azimuthal correlation method [20] (the techniques based on the azimuthal angular correlation between the fission fragments emitted from a rotating compound system should also be cited [21,22] even if they are limited to a narrow beam energy regime). The applicability of all of the above-mentioned methods heavily

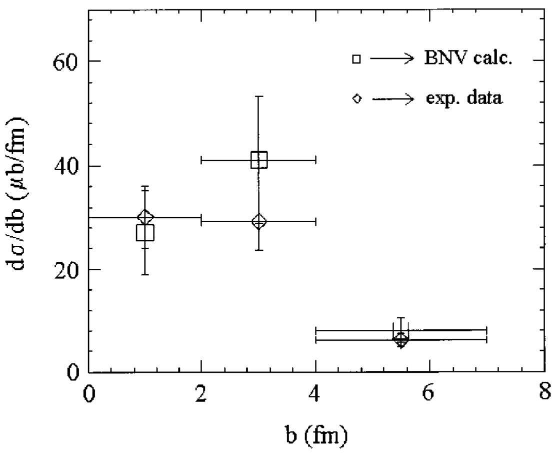

FIG. 11. Impact parameter dependence of pion production cross section relative to the reaction ^{36}Ar+ ^{27}Al at 95 MeV/nucleon.

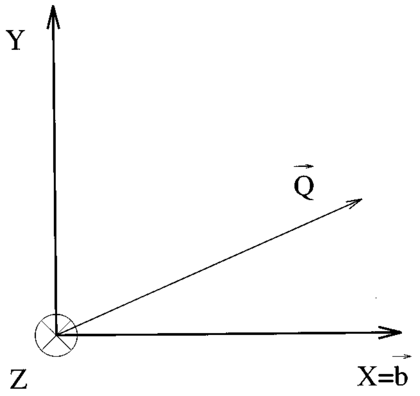

FIG. 13. Graphic representation of the reaction plane. The X-Y system of reference is defined on a plane perpendicular to the beam axis (the beam axis is entering in it along the Z axis). The X axis is parallel to the impact parameter vector.

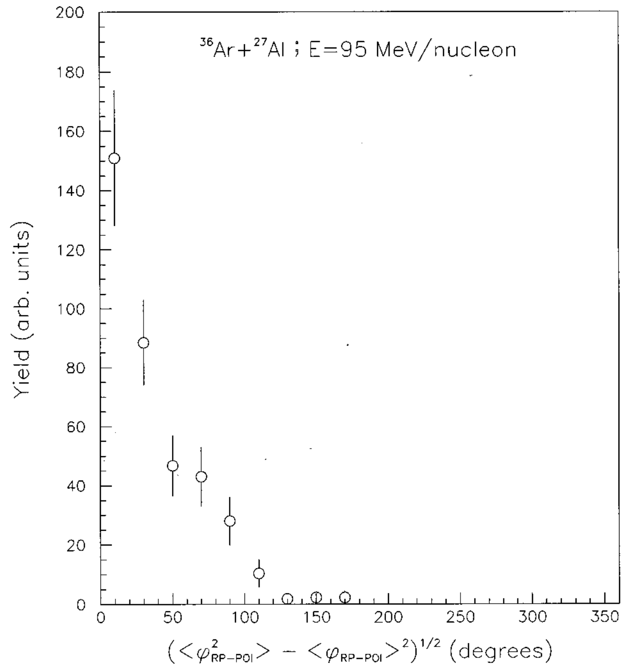

FIG. 14. Distribution of the deviations from the mean of the angle formed by the $\vec{Q}$ vector with the impact parameter vector. Data are relative to the ^{27}Al target.

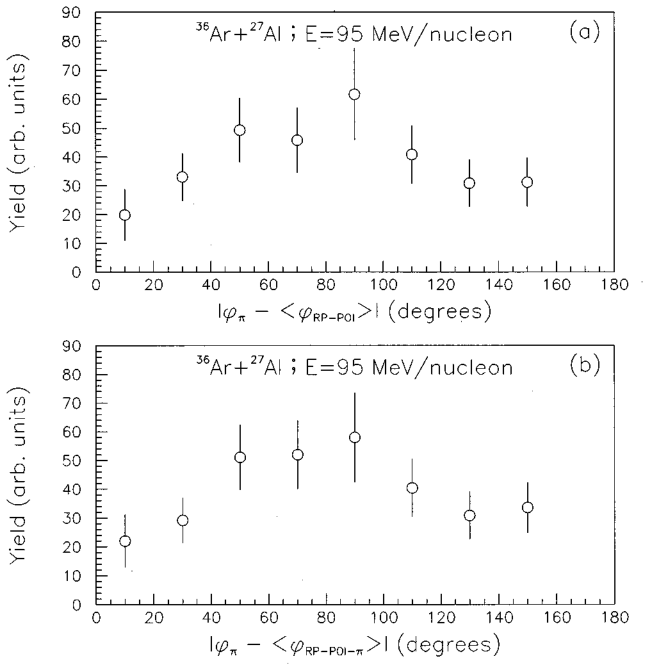

FIG. 16. Azimuthal angular distribution of pions with respect to the reaction plane for the ^{27}Al target. In the upper-panel distribution the $\vec{Q}$ vector has been calculated without the pion boost (see text), while in the lower-panel one this has been included.

relies on the common necessary conditions that (i) the events are *well measured* or (as it is now usual to say) *complete*—i.e., the momenta of *all* particles emitted in each event are precisely determined—and (ii) the problem of defining a reaction plane has a solution—i.e., the impact parameters involved are significantly different from zero. The fulfillment of those conditions is of primary importance for the reliability of the conclusions of this kind of analysis, due to the existence of low-energy thresholds and finite angular acceptance for any real detector. The second one, in particular, has

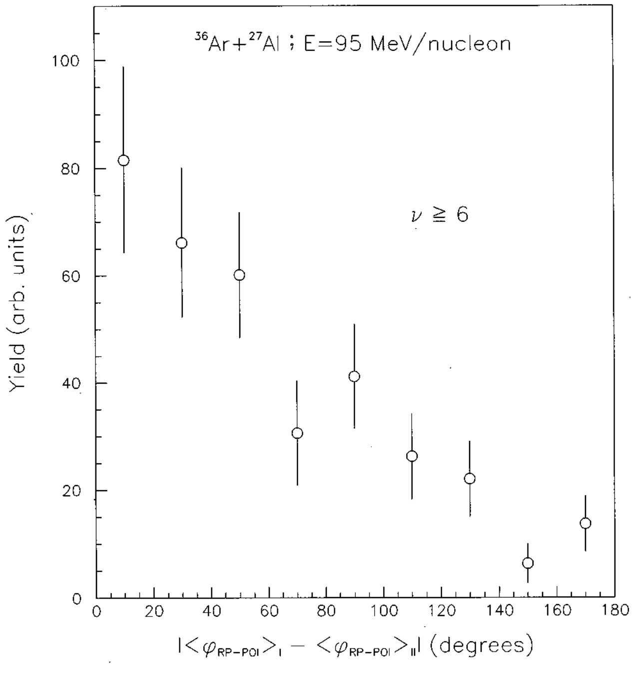

FIG. 15. Distribution of the relative angle between the two vectors $\vec{Q}_I$ and $\vec{Q}_{II}$ calculated with the two subevents I and II (see text). Data are relative to the ^{27}Al target.

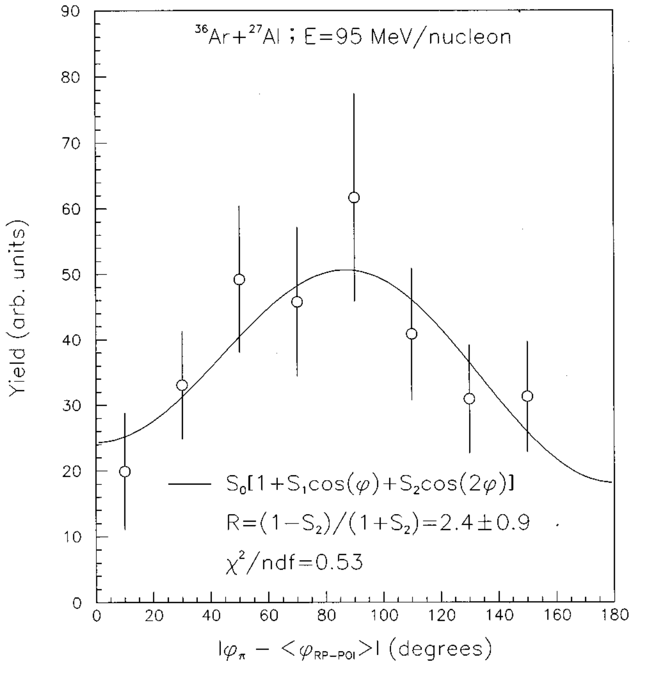

FIG. 17. Comparison between the experimental pion azimuthal distribution relative to the ^{27}Al target and the result of the best-fit procedure discussed in the text using the function defined in Eq. (2).

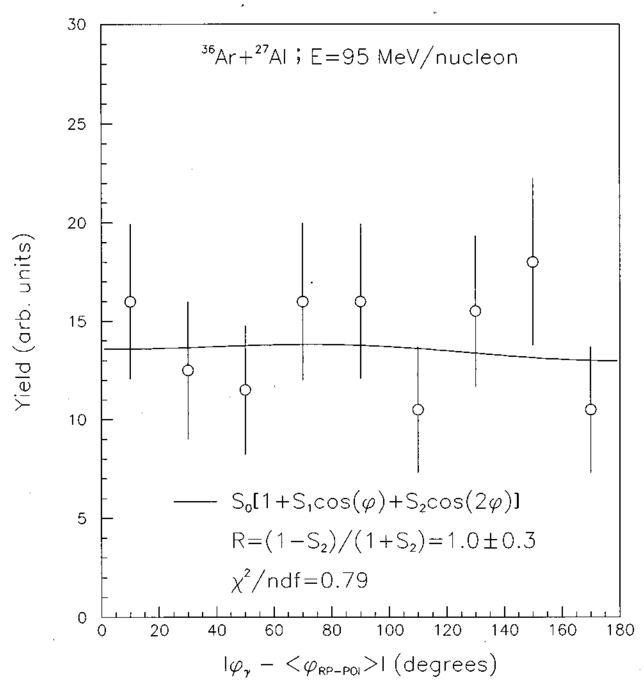

FIG. 18. Comparison between the experimental high-energy photon azimuthal distribution relative to the ^{27}Al target and the result of the best-fit procedure discussed in the text using the function defined in Eq. (2).

to be checked very carefully since it is well known that pions, which are here the particles of interest, are preferentially emitted in central collisions.

All events analyzed in this subsection have been required to verify the *completeness* conditions

$$0.8 < p_{\mathrm{tot}}/p_{\mathrm{proj}} < 1.2 \tag{1}$$

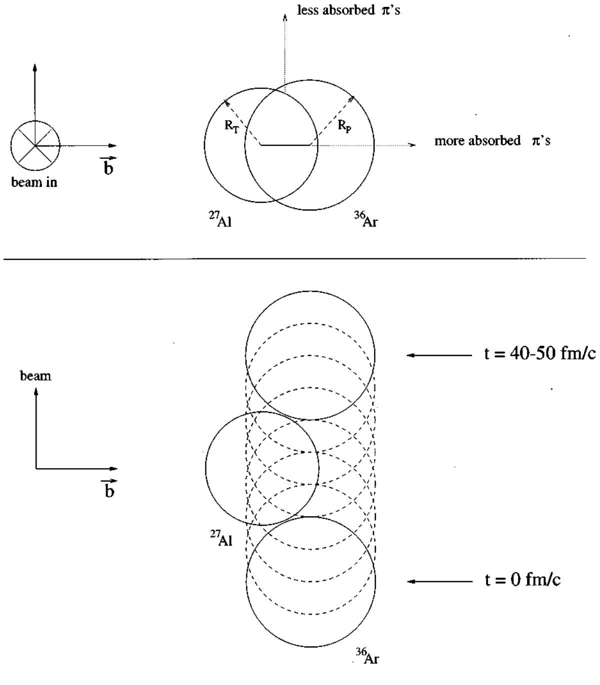

FIG. 19. Geometrical (upper panel) and dynamical (lower panel) pictures of the pion production process.

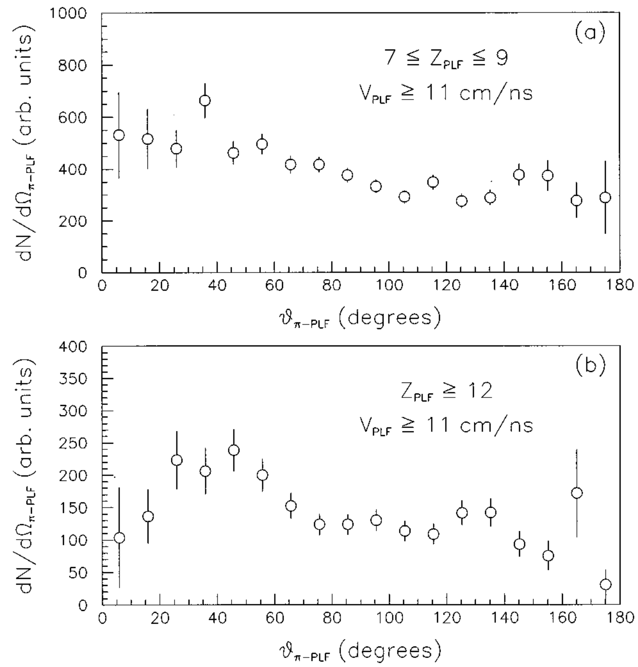

FIG. 20. Distributions of the relative angle between a pion and a PLF. Upper panel refers to PLF's with charge $7 \leqslant Z_{\mathrm{PLF}} \leqslant 9$, while lower panel refers to PLF's with charge $Z_{\mathrm{PLF}} \geqslant 12$. In both panels the lower limit of the PLF velocity is 11 cm/ns. Data are relative to the ^{27}Al target.

and

$$0.8 < Z_{\mathrm{tot}}/(Z_{\mathrm{proj}} + Z_{\mathrm{tgt}}) \leqslant 1, \tag{2}$$

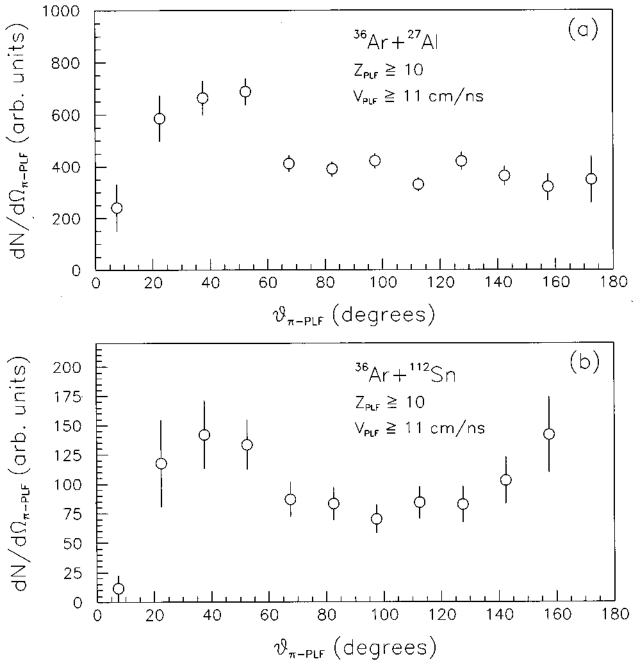

FIG. 21. Distributions of the relative angle between a neutral pion and a PLF having $Z_{\mathrm{PLF}} \geqslant 10$ and $V_{\mathrm{PLF}} \geqslant 11$ cm/ns. The upper panel refers to the ^{27}Al target, while the lower panel refers to the ^{112}Sn target.

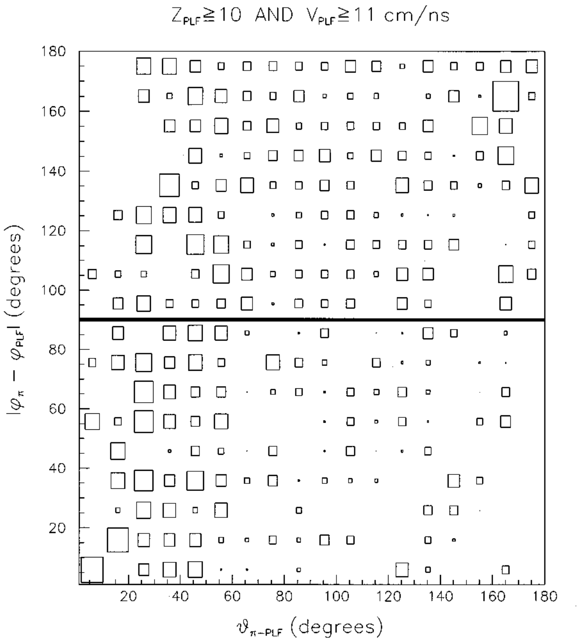

FIG. 22. Event distribution as a function of the relative angle and of the relative azimuthal angle (on a plane perpendicular to the beam axis) between the pion and the PLF. Data are relative to the ^{27}Al target.

where p_{tot} and Z_{tot} are the momentum and the charge, respectively, of all particles detected in the event. The quantity p_{proj} is the projectile momentum while Z_{proj} and Z_{tgt} are the charges of projectile and target, respectively. The event distribution as a function of the total detected charge and linear momentum (normalized to the projectile one) is shown, for the ^{27}Al target, in Fig. 10. The sample of analyzed events is that included in the black-contour box. It represents less than 1% of the total inclusive pion yield (corrected for the detector efficiency).

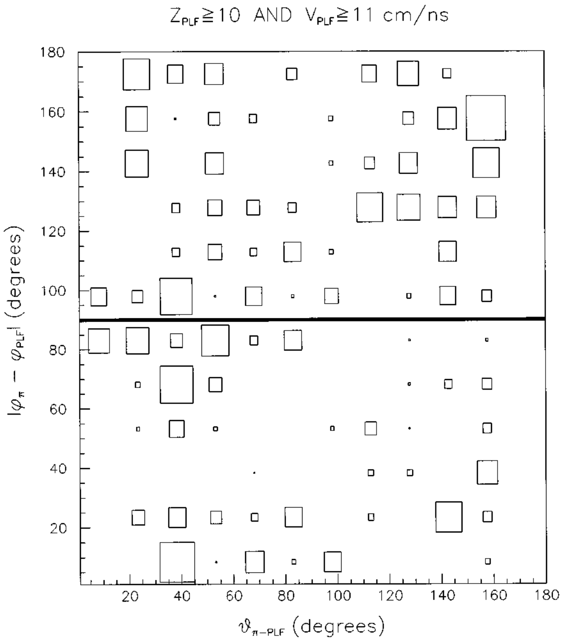

FIG. 23. Event distribution as a function of the relative angle and of the relative azimuthal angle (on a plane perpendicular to the beam axis) between the pion and the PLF. Data are relative to the ^{112}Sn target.

The dependence of subthreshold pion production on the same reaction studied here and at the same bombarding energy has been recently investigated with the same detector in Ref. [7] where the centrality of the collision has been related to the charge particle multiplicity through a procedure based on Monte Carlo simulations [23]. As a summary of the results obtained in that paper, Fig. 11 shows the pion production cross section for the ^{27}Al target as a function of the impact parameter of the collision (a similar plot has been obtained for the heavier target). Impact parameter bins $b=0-2$ fm, $b=2-4$ fm, and $b=4-7$ fm correspond to the charged-particle-multiplicity ranges $\nu>8$, $5<\nu\leqslant 8$, and $1\leqslant\nu\leqslant 4$, respectively. The pion production cross section presents a maximum between $b=1$ fm and $b=3$ fm and then rapidly decreases for more peripheral collisions. Since *complete* events are a very small fraction of all recorded pion events, it is crucial to verify that pion production in these special events has a similar dependence on the impact parameter (i.e., the sample belongs to the same statistical population). Otherwise, the conclusions drawn from the analysis could be not general or, even worse, the determination of the reaction plane could be meaningless. Figure 12 shows the total charged particle multiplicity in *complete* events. The distribution appears shifted to larger values of ν with respect to that reported in Fig. 4 of Ref. [7] which is relative to all pion events. Only the most peripheral bin ($1\leqslant\nu\leqslant 4$), where pion production is still very small, has, however, disappeared while the two most important impact parameter bins have been kept.

If one takes into account a plane perpendicular to the beam axis and defines on it a Cartesian system of reference having the X axis parallel to the impact parameter vector joining the two colliding nuclei and the Y axis orthogonal to it (see Fig. 13), the reaction plane is simply defined by a vector $\vec{Q}$ on that plane. Hence, the reaction plane determination relies on the evaluation of the components of the $\vec{Q}$ vector [19] and/or the angle which it forms with the impact parameter vector [20]. In this work we adopted the transverse momentum analysis of Danielewicz and Odyniec [19] where the $\vec{Q}$ vector is calculated, on an event-by-event basis, as a weighted vectorial sum over the momenta of all fragments detected in the event:

$$\vec{Q}=\left(\frac{1}{\nu}\right)\sum_{i=1}^{\nu}\sum_{j=1,j\neq i}^{\nu} w_j\left(\vec{p}_j^{\,\perp}+\frac{m_j\vec{p}_i^{\,\perp}}{M-m_i}+\frac{m_j\vec{p}_{\pi^0}^{\,\perp}}{M-m_{\pi^0}}\right), \qquad (3)$$

where ν is the current event multiplicity, $M=m_{\mathrm{proj}}+m_{\mathrm{tgt}}$ is the total mass of the interacting system, and w_j is a weight for each particle of mass m_j and rapidity $y_j=(1/2)\ln[(E_j+p_j^{\parallel})/(E_j-p_j^{\parallel})]$ defined as $+m_j$ if $y_j>y_{\mathrm{c.m.}}$ and $-m_j$ if $y_j<y_{\mathrm{c.m.}}$ ($y_{\mathrm{c.m.}}$ is the center-of-mass rapidity). The apex $\perp$ over the particle momentum vectors indicates that only their components orthogonal to the beam axis have been considered. Moreover, in order to be safe from any possible stray angular correlation, particle detection angles (which enter into the calculation of the momentum components) have also been randomized within the angular range

covered by the touched detector. The presence of the term $(1/\nu)$ and of the first summation over the index i means that, for each event, ν reaction planes are determined and then their arithmetic mean is taken. Each time the ith detected particle [usually called particle of interest (POI)] is left out from the second summation over the index j and the $\vec{Q}$ vector is calculated with the other $(\nu-1)$ fragments in the event. The second term between parentheses in Eq. (3) takes into account the momentum boost correction due to the lack of the POI in the event within the hypothesis that the whole system of mass M shared the recoil momentum. The justification of the former assumption is based on the fact that pions are preferentially produced at the very beginning of the collision where the participant matter practically coincides with the whole system. The advantage of this procedure lies in the fact that it allows one to remove the so-called distortion of momenta (see Ref. [19]) which appears if one wants to study the azimuthal angular distribution of a given POI with respect to the reaction plane and includes it into the evaluation of $\vec{Q}$. The third term between parentheses in Eq. (3) takes into account the extra boost due to the momentum of the pion which is created during the reaction and is then absent in the initial state. The quantitative significance of this term will be discussed later on in this subsection.

The most crucial point in the reaction plane determination described by Eq. (3) is that it is evaluated as many times as the event multiplicity (each time removing from the complete event the ith particle of interest) and the final result is the arithmetic mean over the ν different $\vec{Q}$ vectors. The method is, therefore, the more reliable the more the extracted value of $\vec{Q}$ is independent of the particular POI under consideration. That is true only if the error on the mean value is small. Figure 14 reports the distribution of the standard deviations of the angle formed by the $\vec{Q}$ vector with the impact parameter vector. It appears very peaked to zero (as is expected to be) with a mean value of $37.8° \pm 2.6°$. The goodness of the determination of the reaction plane strongly relies on the quality of the event completeness. In our experiment, the multidetector covered the most forward polar angles $(\theta_{\mathrm{min}}=2.5°)$ down to about 3 times the grazing angle for the lighter system $(\theta_g^{\mathrm{Al}}=0.7°)$ and much better for the heavier one $(\theta_g^{\mathrm{Sn}}=1.95°)$. Moreover, the detector granularity in the forward direction $(n_{\mathrm{tot}}=136$ for $\theta<30°)$ is almost 10 times the mean value of the measured charged particle multiplicity in *complete* events $(\overline{\nu}\simeq 13)$. In order to estimate the accuracy of the procedure we randomly divided, following Ref. [19], each event into two subevents (I and II) and compared the reaction planes extracted from these two subevents. In accordance with what has been observed in Ref. [20], only events with a multiplicity greater or equal to 6 have been considered in order to have subevents with at least three fragments. The distribution of the relative angle between the two vectors $\vec{Q}_{\mathrm{I}}$ and $\vec{Q}_{\mathrm{II}}$, calculated with the two subevents, is plotted in Fig. 15 for the ^{27}Al target. The fact that the distribution is not flat testifies to the determination of the reaction plane (compare with Fig. 1 of Ref. [19]).

The azimuthal angular distribution of pions with respect to the reaction plane is reported, for the ^{27}Al target, in Fig. 16. In the upper-panel distribution the $\vec{Q}$ vector has been calculated without the pion boost [the third term between parentheses in Eq. (3)], while in the lower-panel one this has been included. As expected, the contribution from the pion boost is negligible. In both cases, however, it is clearly observable that pions are preferentially emitted in the direction orthogonal to the reaction plane. In order to quantitatively estimate the degree of asymmetry of the azimuthal distribution, in accordance with Refs. [24,25] a best-fit procedure was performed using the function

$$f(\phi)=S_0[1+S_1\cos(\phi)+S_2\cos(2\phi)], \tag{4}$$

where S_0 is an absolute normalization factor, and S_1 and S_2 are two parameters related to the asymmetry of the distribution on the reaction plane and perpendicularly to the reaction plane, respectively. Starting from S_2, it is then possible to define a factor of asymmetry [24,25]:

$$R \overset{\mathrm{def}}{=} \frac{f(90°)+f(270°)}{f(0°)+f(180°)}=\frac{1-S_2}{1+S_2}. \tag{5}$$

By their definitions, of course, $S_2=0$ and $R=1$ mean no asymmetry at all. The result of the best-fit procedure is shown, for the ^{27}Al target, in Fig. 17. The values of the parameters of the best fit as well as those of the reduced χ^2 and of the asymmetry factor R are reported in the second column of Table I. The found values of S_2 and R confirm, within the statistical uncertainties, those extracted by the TAPS Collaboration for the reaction $^{36}\mathrm{Ar}+{}^{197}\mathrm{Au}$ at the same bombarding energy [26], where a completely different method has been used to determine the reaction plane, i.e., the direction of a projectilelike fragment (PLF) having a charge $14<Z_{\mathrm{PLF}}<17$. It is, however, worth noting that while the analysis performed in Ref. [26] concerns only the most peripheral collisions, our treatment uses more central collisions as naturally involved in pion production.

TABLE I. The values of the parameters of the best fit described in the text as well as the values of the reduced χ^2 and of the asymmetry factor R are reported for pion events (second column) and high-energy photon events (third column). Data are relative to the ^{27}Al target.

	π^0 events	γ events
S_0	35.90 ± 3.46	13.52 ± 1.21
S_1	0.087 ± 0.142	0.022 ± 0.126
S_2	-0.408 ± 0.166	-0.018 ± 0.127
χ^2/N_{DOF}	0.53	0.79
R	2.37 ± 0.94	1.03 ± 0.26

The observed *squeeze-out* of pions, with consequent preferential emission normal to the reaction plane, has been recently accounted for by different microscopic theoretical models which explicitly consider pion reabsorption in nuclear matter [27,28]. Up to now, however, the agreement with experimental data is only qualitative and the theoretical interpretation is simply supported by the fact that the bump around $\phi=90°$ appears or disappears as the possibility of pion reabsorption is turned on or off into the calculations. We are here able to give, for the first time, an incontrovertible experimental proof of the fact that pion reabsorption is the mechanism responsible for the azimuthal asymmetry with respect to the reaction plane. We have imposed the same *completeness* conditions discussed before to the high-energy photon events recorded in the same experiment and we have reconstructed the azimuthal distribution with respect to the reaction plane. The result is shown in Fig. 18 together with the best-fit function described in Eq. (4). The values of the S parameters as well as those of the reduced χ^2 and of the asymmetry factor R are reported in the third column of Table I. R is equal to 1 within the statistical error and no asymmetry is indeed observed. The validity of this result is supported by the following arguments. Neutral pion production total cross sections for the studied systems have been found to be more than one order of magnitude smaller than hard photon production total cross sections [16] in agreement with the existing systematics. Moreover, the inclusive multiplicity distribution of high-energy photons ($E_\gamma > 30$ MeV) is strongly peaked to $\nu_\gamma = 1$ and the contribution of two-photon events amounts to a very few percent (in those cases the used multidetector experiences a high efficiency for pion detection and pions are quite easily identifiable and eliminable). Then, a possible source of background in Fig. 18 could be only represented by those events where only one photon coming from neutral pion decay is detected. This is, however, a negligible contribution because (a) the probability of such an event is related to the pion production cross section and, hence, more than a factor of 10 smaller than the photon production cross section, and (b) the detector efficiency for one-detected-photon pion events is about half of that for two-detected-photons pion events. Furthermore, as a result of the negligible interaction of photons with the surrounding nuclear matter, the presence of any structure in Fig. 18 would be explainable by collective effects (such as nucleus-nucleus bremsstrahlung production) in hard photon production which are not expected in heavy-ion collisions in this bombarding energy regime. The flatness of the distribution plotted in Fig. 18 is, to the contrary, a model-independent proof that incoherent nucleon-nucleon collisions play the mayor role responsible for the hard photon production mechanism.

Both pions and high-energy photons are produced in the same class of elementary collisions and the comparison of their azimuthal distributions with respect to the reaction plane then allows one to conclude that the observed asymmetry in the pion distribution is due to the reabsorption of pions in the nuclear matter surrounding the interaction site. Moreover, the analysis of the shape of the distribution plotted in Fig. 17 permits one to extract a simple pictorial view of the collision and quantitatively derive some considerations about its geometry and dynamics. To explain the fact that more pions escape perpendicularly to the reaction plane than on the reaction plane, we have to admit that the two colliding nuclei are significantly aligned along the impact parameter direction and there must be a minimum effective value for b (see the upper panel of Fig. 19). In the case of the lighter studied system, ^{36}Ar and ^{27}Al nuclei have a value of the nuclear radius of 4 fm and 3.6 fm, respectively ($r_0 = 1.2$ fm). So in order to have a geometrical configuration like that shown in the upper panel of Fig. 19 the centers of projectile and target must be shifted by at least twice the difference between their radii, i.e., about 1 fm. Significative pion production should then occur in more peripheral collisions in qualitative agreement with what has been shown in Fig. 11. Besides geometry, also dynamics plays an important role to determine the shape of the pion azimuthal angular distribution. In fact, we also have to admit that the projectile and target are very close to each other when pions come out from the colliding zone. This imposes an upper limit to the time scale of pion emission (see the lower panel of Fig. 19). Starting just after the touching point, pion production should be very close to its end when the emitting source has traveled a distance of the same order of the diameter of the target nucleus (in the lower panel of Fig. 19 the more realistic situation of projectile and target cracking is not, of course, reported). Taking into account the velocity of the nucleon-nucleon center of mass and the sizes of the two interacting nuclei, it is easy to estimate a total pion emission time scale of about 40–50 fm/c.

B. Angular correlation between the pion and PLF

The analysis performed in the previous subsection gives only information about the matter distribution up and down the reaction plane but not on it. The parameter S_1 of the cosine expansion in Eq. (4), which in principle provides a quantitative evaluation of the asymmetry of the pion angular distribution on the reaction plane, is in fact comparable with zero within its error bar (see Table I) and no definitive conclusion can be drawn. Then, in order to improve and deepen the investigation, we have also analyzed the angular correlations between neutral pions and projectilelike fragments detected by the hodoscope of plastic scintillators. Owing to the fact that pions are detected in the whole solid angle starting from the couples of photons coming from their main decay mode, the lower limit in the relative angle between a pion and a PLF is, in this experiment, strictly equal to zero. In the rest of this subsection the condition of *completeness* of the event stated in the previous subsection has been relaxed and substituted with some constraints on both the charge and velocity of the projectilelike fragment.

As an example, two distributions of the relative angle between a pion and a PLF are shown in Fig. 20 for the ^{27}Al target. In both panels the lower limit of the PLF velocity has been set to 11 cm/ns (about 90% of the beam velocity). The upper panel refers to PLF's with charge $7 \leqslant Z_{\mathrm{PLF}} \leqslant 9$, while the lower panel refers to PLF's with charge $Z_{\mathrm{PLF}} \geqslant 12$. As the charge (and size) of the PLF increases, a dip is evidenced in the distribution for small relative angles due to the shadowing induced by the presence of the projectilelike fragment. Beyond an angle of 90°–100° the distributions become rather flat independently of the charge of the projectilelike fragment. Figure 21 shows the other two distributions of the relative angle between a neutral pion and a PLF having $Z_{\mathrm{PLF}} \geqslant 10$ and $V_{\mathrm{PLF}} \geqslant 11$ cm/ns. The upper panel refers to the ^{27}Al target, while the lower panel refers to the ^{112}Sn target. Besides the dips at small relative angles, which are equally present in both distributions with a depth proportional to the target size, it is worth observing here the large-relative-angle part of the two spectra. In the case of the lighter target it is quite flat from $\theta_{\pi\text{-PLF}} = 70°$ up to $\theta_{\pi\text{-PLF}} = 180°$ (as already observed in Fig. 20). In the case of the heavier one, on the contrary, it is flat only in the range

$70° < \theta_{\pi\text{-PLF}} < 130°$, while a strong increase is observed for larger values of the relative angle. The explanation of this effect can be found in the localization of the pion source inside the colliding system. In the case of the ^{27}Al target, the participant region seems, in a first-order approximation, to be roughly spherical, while in the case of the ^{112}Sn target the pion source appears strongly placed in the backward hemisphere and fewer pions are reabsorbed if they are emitted in the opposite direction with respect to the projectilelike fragment. More comprehensive information is provided by the distribution of events as a simultaneous function of the relative angle $\theta_{\pi\text{-PLF}}$ and of the relative azimuthal angle $|\phi_\pi - \phi_{\rm PLF}|$ (on a plane perpendicular to the beam axis) between the pion and the PLF, which is shown in Fig. 22 for the ^{27}Al target and in Fig. 23 for the ^{112}Sn target. Both figures have been obtained imposing the same conditions as in Fig. 21. The thick black lines drawn at $|\phi_\pi - \phi_{\rm PLF}| = 90°$ divide the space in two parts: the near side (closer to the projectile) and the far side (closer to the target). At small relative angles $\theta_{\pi\text{-PLF}} < 30°–40°$ for the lighter target, the shadow of the projectile spectator is clearly observable at large relative azimuthal angles, while some space is left over for the escape of pions in the far side. As the relative angle increases, the situation is turned upside down. The near side is much more populated than the far side where the large masses of the participant and of the target spectator prevent most of the pions from passing through.

The attentive reader should anyhow bear in mind, to catch the meaning of Figs. 20–23, that they do not represent simple *photographs* of the reaction site but rather the superimposition of the frames of a sort of *video tape* taken during the time window in which pions are produced and averaged over a range of impact parameters. This statement is of great importance for a correct understanding of the comparison with theoretical calculations which is presented and discussed in the next section.

IV. COMPARISON WITH A THEORETICAL MODEL

The experimental results discussed in the previous section have been compared with the predictions of a microscopical theoretical model based on the solution of the Boltzmann-Nordheim-Vlasov (BNV) transport equation [2,7,29]. Recently, this model has been successfully used to explain the existing phenomenology of both subthreshold-pion [7,16,17] and hard-photon [16,30] data in heavy-ion collisions at intermediate energies. For a detailed description of the model, the reader is referred to Ref. [2] and references therein.

An important feature of the model, which is here of particular relevance, is the fact that it takes explicitly into account the pion reabsorption [7]. Whenever and wherever a pion is created inside the colliding system, its path is followed inside the nuclear medium, assuming it moves in a straight line determined by its momentum versor $\hat{p}_\pi$. Thus, before escaping from the reaction site, the pion has to travel an effective distance dynamically dependent on the density of the surrounding medium and given by

$$d_{\rm eff}(\vec{r}_\pi,\hat{p}_\pi,t) = \frac{1}{\rho_0}\int_0^{+\infty} \rho(\vec{r}_\pi + \hat{p}_\pi s,t)\,ds, \qquad (6)$$

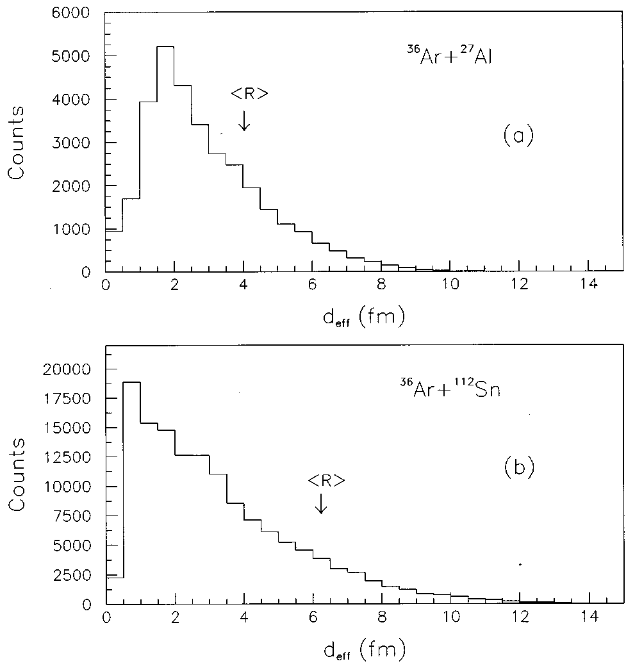

FIG. 24. Comparison between the effective distance distributions predicted by BNV calculations and the sharp values $\langle R \rangle$ coming from the geometrical parametrization described in Ref. [32].

where $(\vec{r}_\pi, t)$ are the pion space-time coordinates, s is the generic length of the pion path, ρ is the nucleon density at the time when the pion is created, and ρ_0 is its saturation value for normal nuclear matter. The pion escape probability is then defined as $P_{\rm esc} = \exp(-d_{\rm eff}/\lambda_0)$ where $\lambda_0 = (\sigma_{\rm abs}\rho_0)^{-1}$ represents the absorption mean-free path in normal nuclear matter. In all the calculations reported in this section we have used the parametrization of Hüfner and Thies [31] for the dependence of λ_0 on the pion kinetic energy. This method of treatment of the pion path inside nuclear matter represents a step forward with respect to what has been made so far. To this respect, Fig. 24 shows the comparison between the effective distance distributions predicted by BNV calculations for the two targets and the sharp values $\langle R \rangle$ calculated using the geometrical parametrization described in Ref. [32]. As an example of the comparison between BNV calculations and experimental data, open squares plotted in Fig. 11 are relative to the prediction of the model for the impact parameter dependence of pion production in the reaction ^{36}Ar+ ^{27}Al at 95 MeV/nucleon.

All the information one can derive from a dynamical model such as BNV about the time dependence of the topology of the collision is contained in the so-called density plots as functions of time, i.e., the distributions of the nuclear matter in the nucleus-nucleus center-of-mass frame at different time steps. The contour plots of the projections on a plane perpendicular to the beam axis of the three-dimensional density distributions relative to the ^{27}Al and ^{112}Sn are reported in Figs. 25, 26 and in Figs. 27, 28, respectively. Figures 25 and 27 refer to calculations performed with an impact parameter $b = 1$ fm, while Figs. 26 and 28 refer to calculations performed with an impact parameter $b = 3$ fm. Those values of b have been chosen because in the

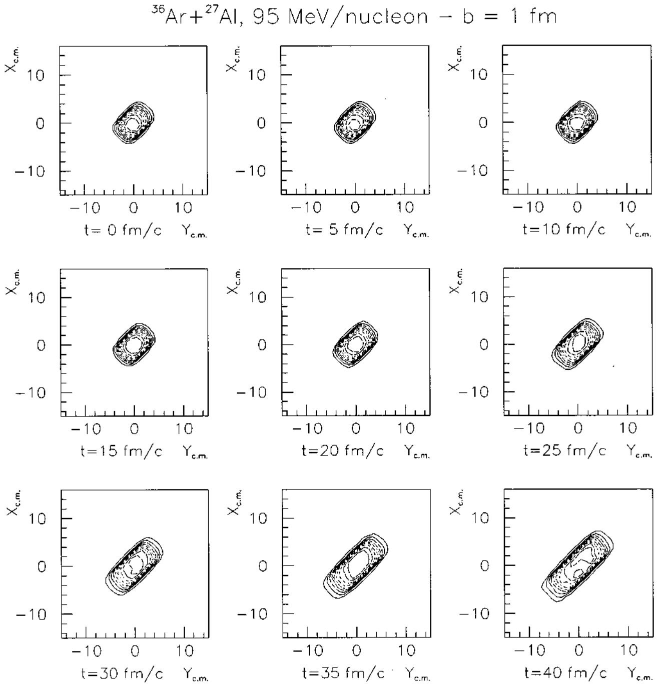

FIG. 25. BNV calculations: the projections of the center-of-mass density distribution on a plane perpendicular to the beam axis are reported for the system ^{36}Ar+^{27}Al at 95 MeV/nucleon at different time steps. The instant $t=0$ is defined as the time when the two colliding nuclei touch each other. The calculations have been performed with an impact parameter $b=1$ fm.

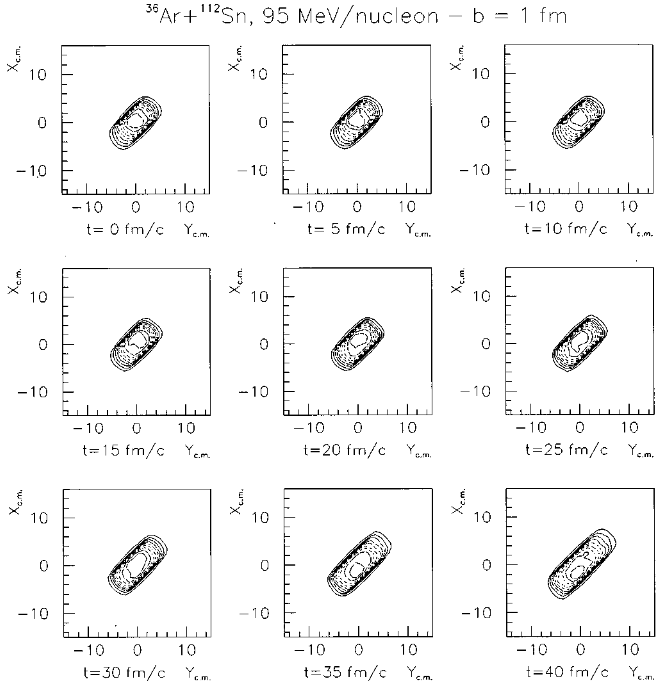

FIG. 27. BNV calculations: the projections of the center-of-mass density distribution on a plane perpendicular to the beam axis are reported for the system ^{36}Ar+^{112}Sn at 95 MeV/nucleon at different time steps. The instant $t=0$ is defined as the time when the two colliding nuclei touch each other. The calculations have been performed with an impact parameter $b=1$ fm.

range $b<4$ fm the model foresees most of the pion production cross section (see Fig. 11). Each of Figs. 25–28 contains nine panels, one for each 5-fm/c time step from $t=0$ to $t=40$ fm/c. The instant $t=0$ is defined as the time when the two colliding nuclei touch each other. The upper limit of 40 fm/c has been chosen looking at the time distribution of the total pion production cross section which is reported, for the ^{27}Al target, in Fig. 29 (a similar picture has been obtained

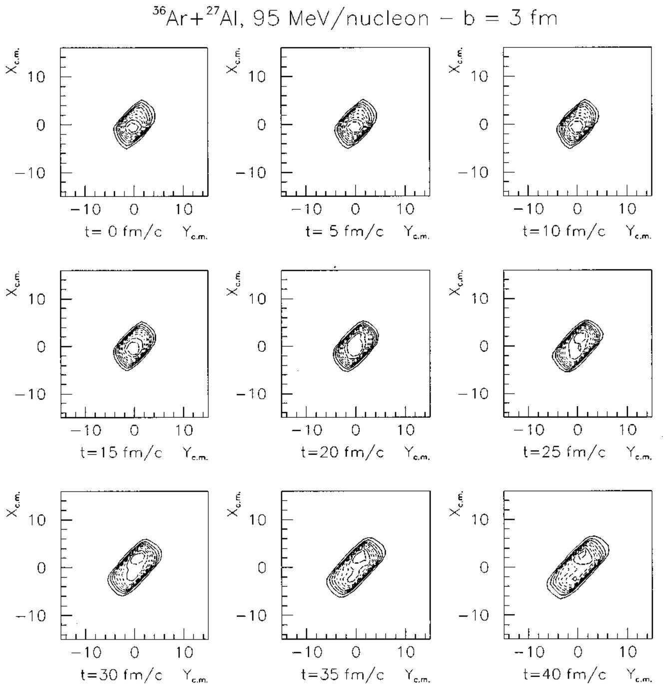

FIG. 26. Same as Fig. 25 with an impact parameter $b=3$ fm.

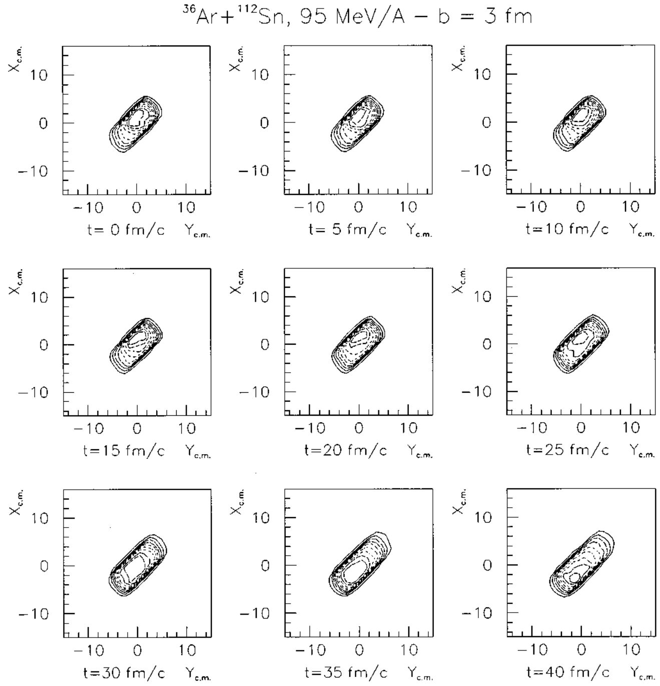

FIG. 28. Same as Fig. 27 with an impact parameter $b=3$ fm.

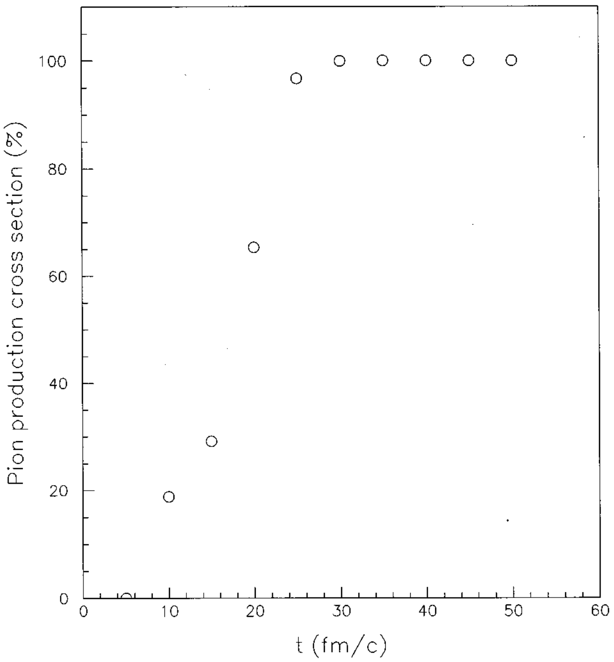

FIG. 29. BNV calculations: the total neutral pion production cross section in the ^{36}Ar+^{27}Al reaction at 95 MeV/nucleon is reported as a function of time.

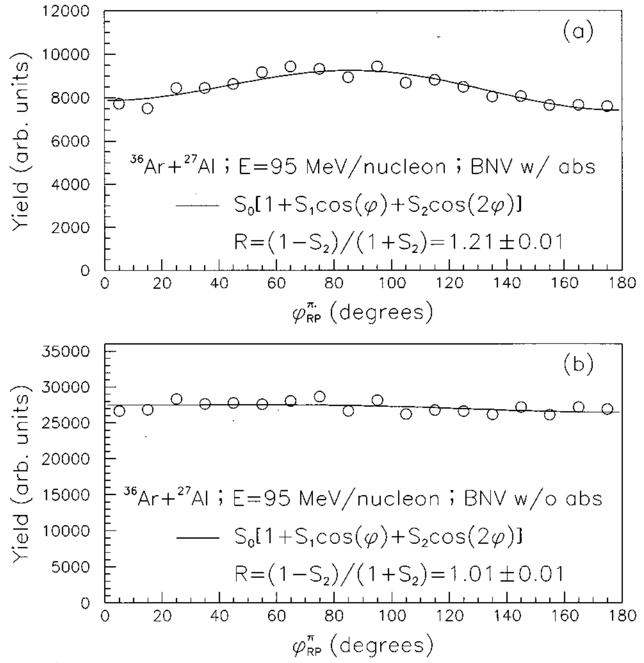

FIG. 30. BNV calculations: the neutral pion azimuthal distribution with respect to the reaction plane is reported for the system ^{36}Ar+^{27}Al at 95 MeV/nucleon. In the upper panel the probability of pion reabsorption is taken into account, while in the lower one it has been set to zero. In both panels the continuous curves refer to the best form of the fit function defined in Eq. (2).

for the heavier target). Most of the pions are created in the time window between 15 fm/*c* and 30 fm/*c*, while at $t=40$ fm/*c* pion production is completely exhausted. It is worth noting how the model reproduces the value of the pion emission time scale extracted in Sec. III from experimental data and justifies the hypothesis made about the elementary production mechanism.

In the time interval in which pions are produced, all density plots evidence a squeezing of the interacting matter, indicating the existence of a reaction plane. The azimuthal angular distribution of pions with respect to the reaction plane has been calculated by the BNV model and it is reported, for the lighter target, in Fig. 30. It is important to stress that the calculation has been integrated over all impact parameters. In the upper panel of the figure the pion escape probability defined before has been considered, while in the lower one it has been set equal to 1 (no reabsorption). In both panels the solid curves refer to the best-fit function defined in Eq. (4). From the relative comparison of the two distributions, it appears evident how the pion azimuthal asymmetry has to be ascribed to the existence of the final state interaction reproducing what we have found experimentally. The flying path in a direction perpendicular to the reaction plane is much shorter than the one parallel to it, even taking into account the fact that in the central region the nuclear density has a calculated value which is about 1.2 times its saturation value. The agreement with data is, however, only qualitative. The extracted theoretical value of the asymmetry factor averaged over all impact parameters ($R=1.21\pm0.01$) is, in fact, only half of that derived from the experiment (even if the experimental value has an error of 40%). A realistic explanation of this discrepancy can be found in the fact that the model does not contain, in its present form, either multiple creation-absorption steps or the pion rescattering whose size could be of the same order of magnitude of reabsorption. Moreover, the reaction plane is not calculated using the same procedure defined for experimental data, i.e., starting from the momenta of all particles emitted in the event, but it is given by the model itself. Because of the one-body character of the distribution function entering in the transport equation, that problem is, however, insurmountable. Complex fragments are not defined at all in the model and it is not then possible to make an event generator of it.

The localization of the pion source and the distribution of nuclear matter on the reaction plane as a function of time can also be studied by the BNV model looking at the density-plot projections on a plane containing the beam axis and the impact parameter vector. The contour plots of these projections are shown in Figs. 31 and 32 for the ^{27}Al target and in Figs. 33 and 34 for the ^{112}Sn target. Figures 31 and 33 refer to calculations performed with an impact parameter $b=1$ fm, while Figs. 32 and 34 refer to calculations performed with an impact parameter $b=3$ fm. The half-plane with $X_{\mathrm{c.m.}}>0$ is the near side while that with $X_{\mathrm{c.m.}}<0$ is the far side. It is straightforward to observe how the density plots reported in the panels at the time steps between $t=15$ fm/*c* and $t=30$ fm/*c* clearly explain the observation of enhanced/reduced absorption in selected directions.

V. SUMMARY AND CONCLUSIONS

Pion shadowing due to the strong absorption effect has been used as a powerful tool to study the topology of heavy-ion collisions at intermediate energies. Pions have been used just like *x rays* to obtain, as a function of time, some *radio-*

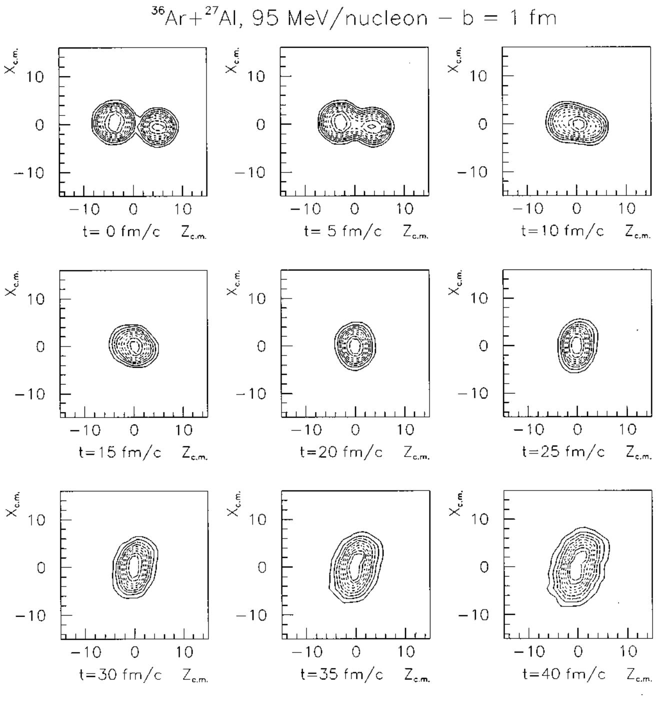

FIG. 31. BNV calculations: the projections of the center-of-mass density distribution on a plane containing the beam axis (the Z axis) and the impact parameter vector (parallel to the X axis) are reported for the system ^{36}Ar+ ^{27}Al at 95 MeV/nucleon at different time steps. The calculations have been performed with an impact parameter $b=1$ fm.

graphs of the spatial distribution of the interacting nuclear matter all around the reaction site. The analysis of the azimuthal angular distribution with respect to the reaction plane and of the angular correlation between pions and projectile-like fragments has allowed us to estimate the pion production time scale and to establish a lower limit in the impact parameter.

The experimental results have been successfully com-

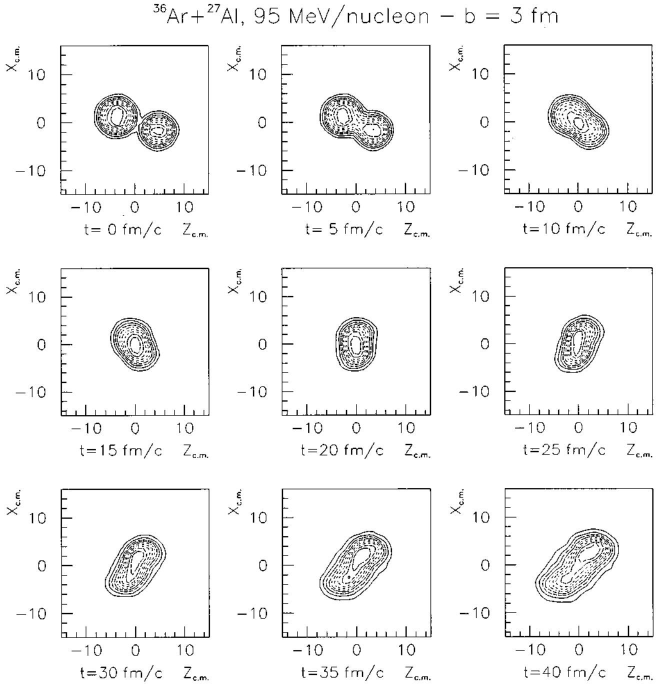

FIG. 32. Same as Fig. 31 with an impact parameter $b=3$ fm.

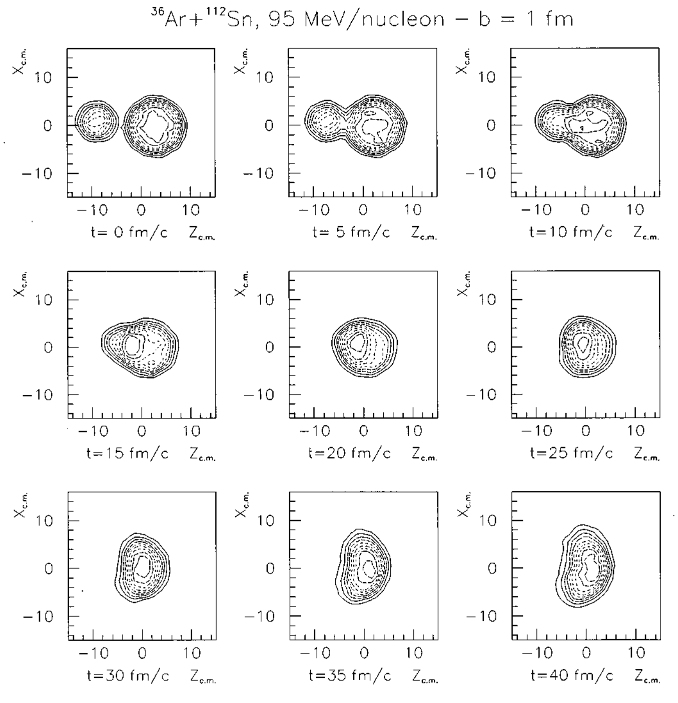

FIG. 33. BNV calculations: the projections of the center-of-mass density distribution on a plane containing the beam axis (the Z axis) and the impact parameter vector (parallel to the X axis) are reported for the system ^{36}Ar+ ^{112}Sn at 95 MeV/nucleon at different time steps. The calculations have been performed with an impact parameter $b=1$ fm.

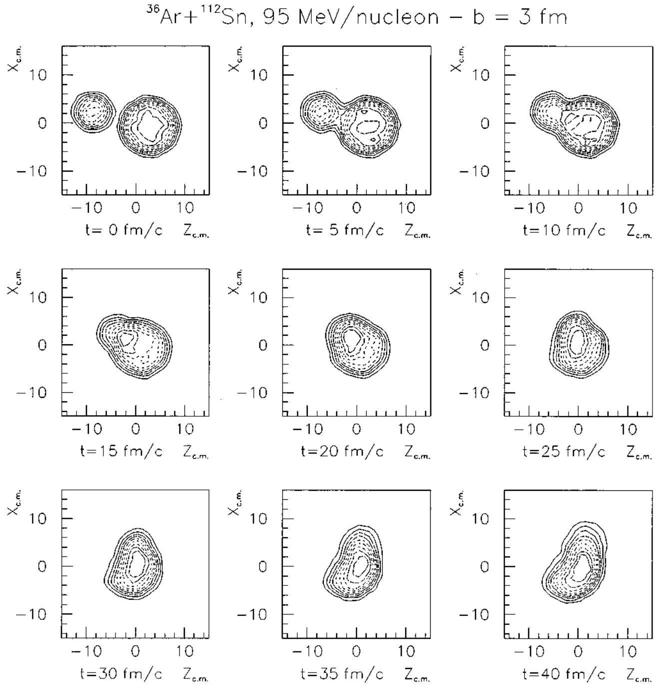

FIG. 34. Same as Fig. 33 with an impact parameter $b=3$ fm.

pared with the predictions of a microscopic theoretical model, based on the solution of the Boltzmann-Nordheim-Vlasov transport equation, which takes into account pion reabsorption in a dynamical way. Theoretical calculations give a good description of the observed phenomenological evidence, but a more refined treatment of pion final state interactions in nuclear matter has to be realized to attain a better quantitative agreement.

[1] W. Cassing, V. Metag, U. Mosel, and K. Niita, Phys. Rep. **188**, 365 (1990).

[2] A. Bonasera, F. Gulminelli, and J. J. Molitoris, Phys. Rep. **243**, 1 (1993).

[3] For a review, see D. Ashery and J. P. Schiffer, Annu. Rev. Nucl. Part. Sci. **36**, 207 (1986), and references therein.

[4] P. Hecking, Phys. Rev. B **103**, 401 (1981).

[5] W. Cassing, Z. Phys. A **329**, 487 (1988).

[6] R. S. Mayer *et al.*, Phys. Rev. Lett. **70**, 904 (1993).

[7] A. Badalà *et al.*, Phys. Rev. C **48**, 2350 (1993).

[8] E. Migneco *et al.*, Nucl. Instrum. Methods Phys. Res. A **314**, 31 (1992).

[9] T. Murakami, J. Kasagi, H. Tachibanaki, K. Yoshida, Y. Shibata, T. Nakagawa, M. Ogihara, S. M. Lee, T. Kubo, and T. Motobayashi, Nucl. Instrum. Methods Phys. Res. A **253**, 163 (1986).

[10] A. Del Zoppo *et al.*, Nucl. Instrum. Methods Phys. Res. A **327**, 363 (1993).

[11] A. Badalà, R. Barbera, A. Palmeri, G. S. Pappalardo, F. Riggi, and A. C. Russo, Nucl. Instrum. Methods Phys. Res. A **306**, 283 (1991).

[12] G. Bellia *et al.*, Nucl. Instrum. Methods Phys. Res. A **329**, 173 (1994).

[13] CERN Application Software Group, GEANT: *Detector Description and Simulation Tool* (CERN, Geneva, 1993); CERN Program Library Long Writeups W5013.

[14] A. Badalà, R. Barbera, A. Palmeri, G. S. Pappalardo, F. Riggi, A. C. Russo, G. Russo, and R. Turrisi, Nucl. Instrum. Methods Phys. Res. A **351**, 387 (1994).

[15] A. Badalà, R. Barbera, A. Palmeri, G. S. Pappalardo, F. Riggi, A. C. Russo, G. Russo, and R. Turrisi, Nucl. Instrum. Methods Phys. Res. A **357**, 443 (1995).

[16] A. Badalà, R. Barbera, A. Palmeri, G. S. Pappalardo, F. Riggi, A. C. Russo, G. Russo, and R. Turrisi, Phys. Rev. C **55**, 2521 (1997), the following paper.

[17] A. Badalà *et al.*, Phys. Rev. C **47**, 231 (1993).

[18] M. Gyulassy, K. A. Frankel, and H. Stöcker, Phys. Lett. **110B**, 185 (1982).

[19] P. Danielewicz and G. Odyniec, Phys. Lett. **157B**, 146 (1985).

[20] W. K. Wilson, R. Lacey, C. A. Ogilvie, and G. D. Westfall, Phys. Rev. C **45**, 738 (1992).

[21] M. B. Tsang *et al.*, Phys. Rev. Lett. **57**, 559 (1986).

[22] R. P. Schmitt and B. K. Srivastava, Z. Phys. A **335**, 49 (1990).

[23] A. Badalà, R. Barbera, A. Palmeri, G. S. Pappalardo, F. Riggi, and A. C. Russo, Z. Phys. A **344**, 455 (1993).

[24] D. Brill *et al.*, Phys. Rev. Lett. **71**, 336 (1993).

[25] L. B. Venema *et al.*, Phys. Rev. Lett. **71**, 835 (1993).

[26] A. Schubert *et al.*, Phys. Lett. B **328**, 10 (1994).

[27] S. A. Bass, C. Hartnack, H. Stöcker, and W. Greiner, Phys. Rev. Lett. **71**, 1144 (1993).

[28] B. A. Li, Phys. Lett. B **319**, 412 (1993).

[29] A. Bonasera, G. Russo, and H. H. Wolter, Phys. Lett. B **246**, 337 (1990).

[30] E. Migneco *et al.*, Phys. Lett. B **298**, 46 (1993).

[31] J. Hüfner and M. Thies, Phys. Rev. C **20**, 273 (1979).

[32] W. Cassing, Z. Phys. A **329**, 487 (1988).